Journal of Materials Chemistry

Cite this: *J. Mater. Chem.*, 2012, **22**, 1998

www.rsc.org/materials

PAPER

Interface synthesis of gold mesocrystals with highly roughened surfaces for surface-enhanced Raman spectroscopy†

Hongjun You, Yuetian Ji, Liang Wang, Shengchun Yang,* Zhimao Yang, Jixiang Fang,* Xiaoping Song and Bingjun Ding

Received 11th July 2011, Accepted 26th October 2011
DOI: 10.1039/c1jm13211c

Local electromagnetic enhancement excited from collective oscillations of free electrons on a highly roughened mental surface can induce greatly enhanced Raman scattering. Herein gold mesoparticles with various morphologies and highly roughened surfaces, including sea urchin-like, flower-like, star-like, meatball-like, and dendritic nanostructures are prepared using pentanol/water interface as a growth "bed". The morphologies of the prepared gold mesoparticles are well controlled by varying the concentrations of additives such as gold ions, ascorbic acid (AA) and cetyltrimethylammonium bromide (CTAB). Due to the unique structures such as rough surface, high internal porosity as well as complex morphology, these as-prepared mesocrystals exhibit a remarkable performance in surface-enhanced Raman scattering (SERS) compared with polyhedral mesoparticles.

1. Introduction

Surface-enhanced Raman scattering (SERS) is a powerful spectroscopic technique that can provide non-destructive and ultrasensitive analysis at the single molecular level, which can be widely applied in biochemistry, chemical production, and environmental monitoring.[1–7] SERS involves two different mechanisms. One is the chemical enhancement caused by the charge transfer between a molecule and an adjacent metal surface,[8,9] The other is the local electromagnetic enhancement that originates from the excitation of the collective oscillations of free electrons in noble or transition metals.[10–12] The plasmonic coupling effect at the nanometre gap junction between particles induces very high local electromagnetic enhancement, which generates "hot spots" with high SERS enhancement (more than 10^{10}), even for single molecule detection.[13–19] But the reproducibility of "hot spots" is difficult to achieve because each "hot spot" is small in size and therefore the quality of the SERS enhancement varies.[14] For instance, in the SERS signal distribution measurements with silver nanospheres, 63 SERS active sites of 1×10^6 sites contributed 24% of the overall SERS intensity.[20] Thus the large area SERS enhancement of a rough surface fabricated with random "hot spots" usually is on the order of 10^2–10^6.[21] To obtain stable and reproducible SERS enhancement, periodic nanostructures fabricated with nanometre-scale lithography techniques have been developed and widely studied,[22] but small gaps (*e.g.*, <10 nm) in the above periodic nanostructures are difficult to achieve in these techniques. Recently, the hierarchical 3D nanostructure with a rough surface on a metal mesoparticle has induced much research interest because a SERS enhancement with intensity over 10^7 was obtained with a relatively high reproducibility.[23] Because abundant bright "hot spots" can be generated on individual hierarchical particles, a very high reproducibility of the SERS substrate can be obtained.[24] Furthermore, if the hierarchical mesoparticles are assembled together, more "hot spots" can be generated between particles.[23]

Up to now, various methods have been developed to synthesize metal hierarchical particles in wet chemical systems. A series of silver or gold hierarchical 3D mesoparticles such as sea urchin-like,[23] flower-like,[25] meatball-like,[26] and star-like[17] morphologies have been reported, which exhibited strong enhancement in SERS. Several mechanisms are involved in the hierarchical particles growth such as the anisotropic growth induced by a twin plane,[27,28] specific capping agents,[29,30] kinetic effects,[31–33] etching,[17,34,35] and particle-mediated growth.[36–38] Different from atom/ion mediated growth, particle-mediated growth is a non-classical pathway of crystallization deduced by Cölfen *et al.* from biomineralization.[39,40] This mechanism is based on oriented attachment (OA)[41] of crystal building units and results in the formation of so-called "mesocrystals".[42] Mesocrystals are ordered mesoscale superstructures composed of individual nanocrystals that are aligned along a common crystallographic direction, exhibiting scattering properties similar to those of a single crystal.[43] Recently metal hierarchical particles formed by particle-mediated growth have been explored in many systems[40]

MOE Key Laboratory for Non-equilibrium Synthesis and Modulation of Condensed Matter, State Key Laboratory for Mechanical Behavior of Materials, School of Science, Xi'an Jiaotong University, Shann Xi, 710049, People's Republic of China. E-mail: ysch1209@mail.xjtu.edu.cn; jxfang@mail.xjtu.edu.cn

† Electronic Supplementary Information (ESI) available: Fig. S1, S3–5, S7–8 and S10–12, larger area SEM images of gold mesoparticles with different morphologies; Fig. S2, S6 and S9, Size distribution histograms of different gold mesoparticles. See DOI: 10.1039/c1jm13211c

in which small nanoparticle (NP) units aggregate through an OA process to form porous or dendritic hierarchical structures.[44–46] Besides SERS substrates, metal hierarchical particles have been synthesized for a wide range of technological applications such as nanocircuits and nanodevices,[47] catalysts for proton-exchange membrane (PEM) fuel cells,[48] electrochemistry or photo-catalysts,[49] and left-handed materials (LHMs),[50] *etc.*

In this paper, a pentanol/water interface was developed as a growth bed to synthesize gold hierarchical mesoparticles based on previous reports by Wang and by our group.[51–53] By controlling synthetic parameters, gold mesoparticles with sea urchin-like, star-like, flower-like, meatball-like and dendritic hierarchical morphologies could be obtained. The mesoparticles could further self-connect each other on the interface to form a particle-monolayer film which served as a substrate showing excellent SERS properties. The current oil/water interface synthesis shows two remarkable advantages: 1) compared with solid/solution interface synthesis, the product can be more easily transferred. The solid/solution interface is also commonly used to prepare metal films, but the films are difficult to transfer to other substrates. In our oil/water interface synthesis, the film can be easily transferred onto any substrate and even can be dispersed into solutions; 2) compared with solution synthesis, the product can be more easily self-connected to form a particle-monolayer film on the solution surface, while in the solution synthesis, the self-assembly of metal nanoparticles is difficult.

2. Experimental section

2.1 Synthesis of gold mesoparticles

In a typical synthesis of Au mesostructures, as shown in Fig. 1, 1.5 ml of $HAuCl_4$ aqueous solution (20 mM) and 0.5 ml of chloroform were mixed in a 6 ml glass vial followed by vibrating for 20 s. Then 2 ml of pentanol was added into the vial and mixed by vibrating for 10 min. After the vial was put in the dark for 1 day, the solution in the vial was separated into two layers: a yellow upper layer and a colorless bottom layer, indicating that all of the $HAuCl_4$ was extracted into the upper pentanol solution layer. A mixed solution of 20 ml of deionized (DI) water and 1.5 ml of ascorbic acid (AA) aqueous solution with different concentrations was poured into a glass Petri dish, and then 5 ml of pentanol was added into the water solution. Two layers were formed in the Petri dish: the upper layer was pentanol solution and the bottom one was water solution containing AA (Fig. 1a). After the solution was stable, 0.5 ml of pentanol solution containing $HAuCl_4$ (previously prepared in a vial) was slowly injected into the upper pentanol solution layer along the Petri dish wall. After several minutes, some opaque orange products appeared at the interface and gradually became red and then dark red, indicating the reduction reaction happened and the Au particles formed with $AuCl_4^-$ ions and AA molecules diffusing toward the interface (Fig. 1b). The reaction lasted for 5 h. After the reaction, the upper pentanol layer was removed and the gold particles self-connected to form a particle-monolayer film on the water solution surface. The products were further characterized with scanning electron microscopy (SEM) or high-resolution transmission electron microscopy (HRTEM/TEM) (Fig. 1b).

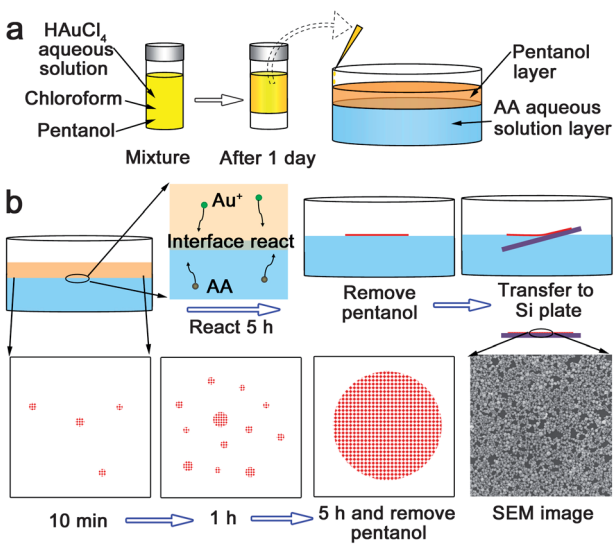

Fig. 1 Schematic of gold mesoparticles being synthesized at the pentanol/water interface. (a) Gold precursor is extracted into pentanol solution and (b) evolution of gold product at the interface.

2.2 Material characterization

The morphology of the products was investigated by field emission scanning electron microscopy (FE-SEM) using a JEOL (JSM-7000F) at an accelerating voltage of 20 kV. The transmission electron microscopy (TEM) and high-resolution transmission electron microscopy (HRTEM) analysis images as well as selected-area electron diffraction (SAED) pattern analysis were performed on a JEOL JEM-2100 transmission electron microscope operating at an accelerating voltage of 200 kV.

2.3 SERS measurement

SERS measurements were carried out on a confocal microprobe Raman spectrometer (LabRAM HR800, HORIBA JOBIN YVON) with the 633 nm He–Ne laser line at room temperature. The probe area was 1 μm in diameter with a ×100 objective lens and the signal collection time was 1 s. The incident power of the laser at the samples was 0.055 mW after it was decreased by a D2 attenuation piece. The products transferred onto a cleaned quartz plate were used for SERS sample preparation . Samples for SERS were prepared by drop casting 25 μL of 1×10^{-5} M rhodamine 6G (R6G) aqueous solution on the quartz plate and allowing the solvent to evaporate.

3. Results and discussion

3.1 Sea urchin-like gold mesoparticles

Fig. 2 and S1† show the SEM images of sea urchin-like mesoparticles which are uniformly coated by a highly roughed surface. The size is around 125 ± 27 nm (Fig. S2†) which is much smaller than the sea urchin-like gold mesoparticles prepared with the galvanic method as reported in our previous work.[23] The SEM image of a single mesoparticle (inset of Fig. 2a) shows that its surface is covered by closely packed spikes. The density of the spikes on a single particles (number of spikes per area) is estimated to be 10 times higher than that shown in our previous

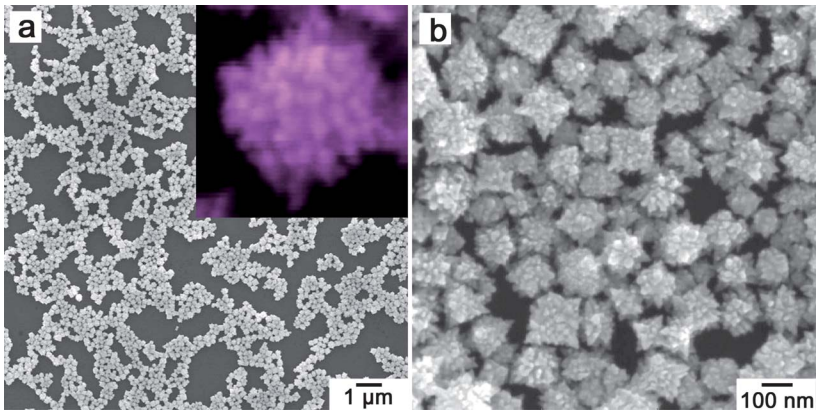

Fig. 2 SEM images of gold sea urchin-like mesoparticles synthesized with 100 mM AA and 20 mM gold precursor. (a) Large area and (b) magnified SEM images. The inset in (a) shows a typical SEM image of a gold sea urchin-like mesoparticle.

work,[23] assuming the number of tips is 100 and 200 in this case and previous reports, respectively (the corresponding average particle sizes are 150 and 700 nm, respectively). The SEM image also shows that the film is a particle-monolayer which automatically forms on the water surface.

The TEM, HRTEM images and SAED patterns of the gold sea urchin-like mesoparticles provide further details in structure analysis as shown in Fig. 3. The highly textured mesoparticles are clearly covered with many small spikes with lengths from 30 to 60 nm and base thicknesses from 8 to 15 nm (Fig. 3a, b), which is much smaller than those in our previous report (base thickness of 30–50 nm).[23] The TEM image contrast of a single particle shows an incompact structure. Similar to other reports,[36,44,45] the mesoparticle should be formed by particle-mediated growth. The broadening of SAED spots, especially for that of the high-index crystal planes, suggest a common orientation with a small angle lattice mismatch between the primary NP building units. The HRTEM image shown in Fig. 3c recorded from the cycled area of Fig. 3b further supports this suggestion in which three spikes grow from the tips of mesocrystal separately, while they share the same crystalline orientation. The lattice space in the HRTEM (Fig. 3c) is 0.233 nm, which matches well with Au {111} planes *d*-spacing (0.235 nm), indicating an overgrowth along the <111> crystallographic orientations. This growth behavior is very similar to the formation of PtRu alloy mesoparticles in an organic solvent at high temperature as reported by Yang and coworkers,[36] in which the primary NPs are mainly covered by lowest energy facets and their oriented attachment preferentially occurs on these {111} lowest energy facets, as illustrated in Fig. 3d.

3.2 Morphology evolution of gold mesoparticles

3.2.1 Effect of gold precursor concentration. In our experiments, the effects of different synthesis conditions on the morphologies of gold mesoparticles were systematically investigated. Fig. 4 shows the morphology transformation of gold mesoparticles obtained at different gold precursor concentrations. Compared with the mesoparticles in Fig. 2, at a lower value, the size of products decreases from 125 nm to 106 nm (Fig. 4c), and the diameter of spikes decreases to around 10 nm (Fig. 4a and b). Instead, when the concentration of $AuCl_4^-$ ions in the pentanol phase is increased to a higher value, the SEM images show that the obtained mesoparticles consist of two different size distributions (Fig. 4d–f and S3†), of which the smaller and larger mesoparticles have average diameters of around 160 nm and

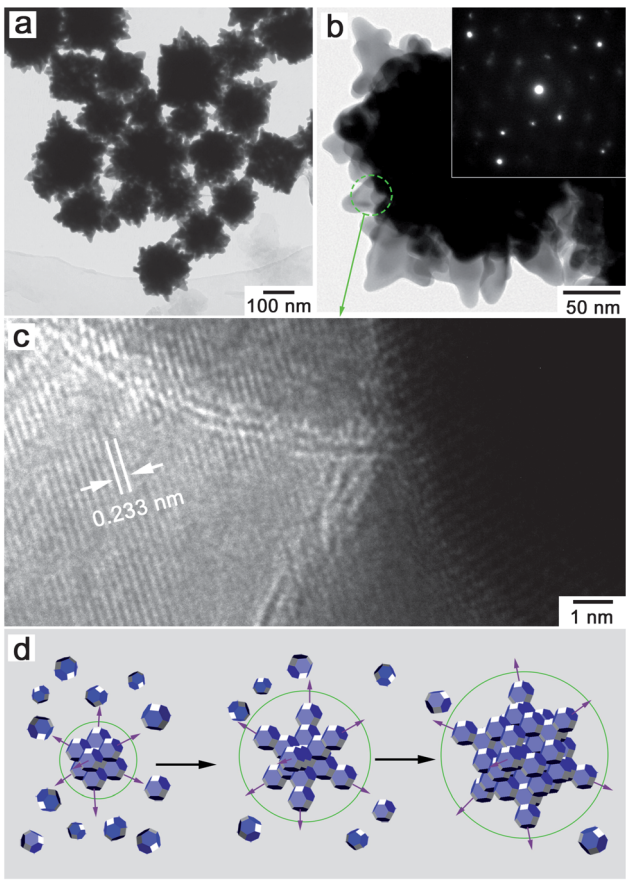

Fig. 3 TEM and HRTEM images of gold sea urchin-like mesoparticles and the illustration scheme for the hierarchical 3D structure formation. (a) TEM image of large area of gold mesoparticles. (b) TEM image of a single typical mesoparticle. The inset shows the correlated SAED patterns. (c) HRTEM images of the circled area in (b). (d) Illustration of mesocrystal formation by the primary NPs oriented attachment.

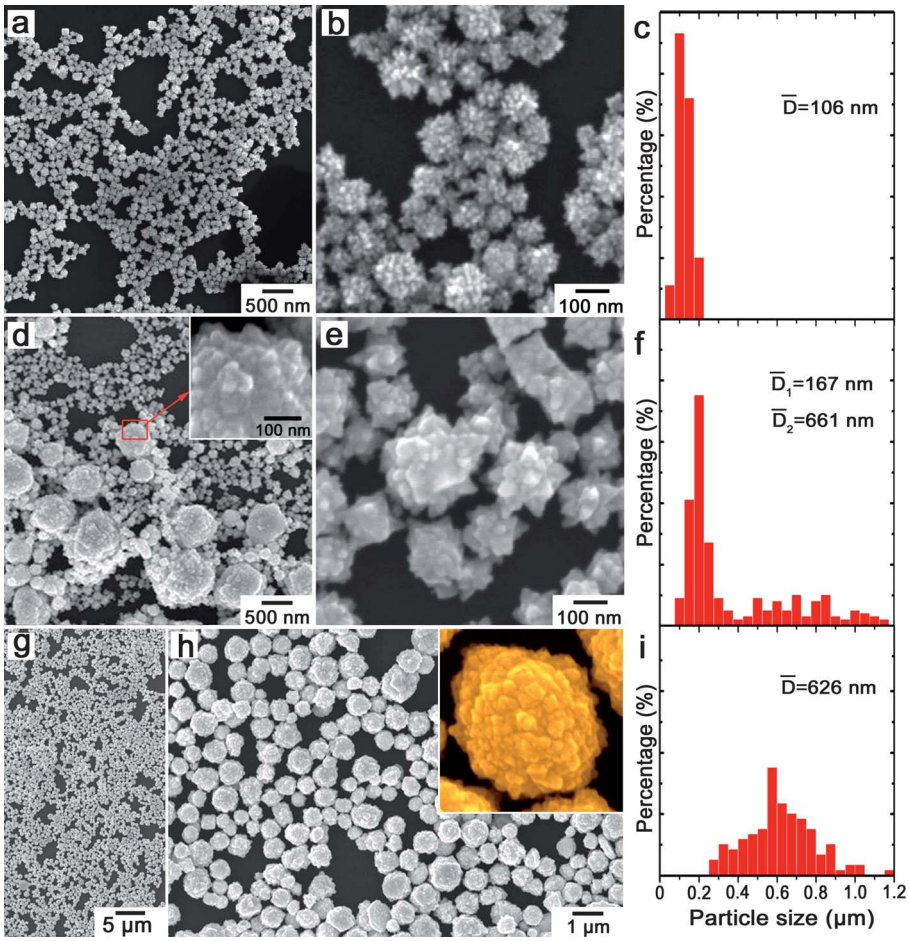

Fig. 4 Different magnified SEM images of gold mesoparticles synthesized with the same AA concentration (100 mM) and different gold precursor concentrations: (a, b) 10 mM, (d, e) 50 mM, and (g, h) 100 mM. (c, f, i) The correlated size distribution histograms of different gold mesoparticles.

660 nm, respectively. Although the average diameters of these two types of mesoparticles are obviously different, the sizes of the building units involved in both of them are almost identical (around 25 nm). These bimodal particles exhibit quite different morphologies as shown in Fig. 4d and e: the larger mesoparticle is meatball-like and the smaller one is star-like. When the concentration of Au ions was further increased to100 mM, only meatball-like mesoparticles with an average size of 626 nm (Fig. 4i) were obtained (Fig. 4g, h and S4†).

3.2.2 Effect of AA and CTAB concentration. The concentration of reducing agent (AA) also has an important effect on the morphology evolution of gold mesoparticles. Fig. 5 and S5† show the SEM images of gold mesoparticles synthesized at different AA concentrations. As one can see, the star-like gold mesoparticles dominated in the products when the AA concentration was 20 mM (Fig. 5a and S5a†), and the overgrowth of their tips led to the formation thicker spikes on the particle surface. When AA concentration was increased to 1 M, the surface of gold mesoparticles is mainly covered by densely distributed tiny spikes, as shown in Fig. 5b and S5b.†

The morphology of gold mesoparticles can also be well controlled by adding a certain amount of CTAB in the pentanol phase and choosing an appropriate AA concentration in the aqueous phase. For instance, when the AA concentration was kept at 20 mM, the addition of CTAB into the pentanol phase obviously led to the formation of polyhedral nanoparticles. As shown in Fig. 6a and S6,† only gold polyhedral nanoparticles with an average size of 96 ± 15 nm can be observed in the products rather than the star-like mesoparticles. When the concentration of CTAB in the pentanol phase was further increased to 40 mM, the Au polyhedra showed a tendency to

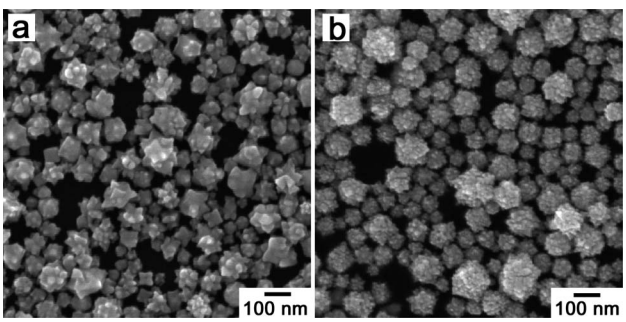

Fig. 5 SEM images of gold mesoparticles synthesized with the same gold precursor concentration (20 mM) and different AA concentrations: (a) 20 mM, (b) 1 M.

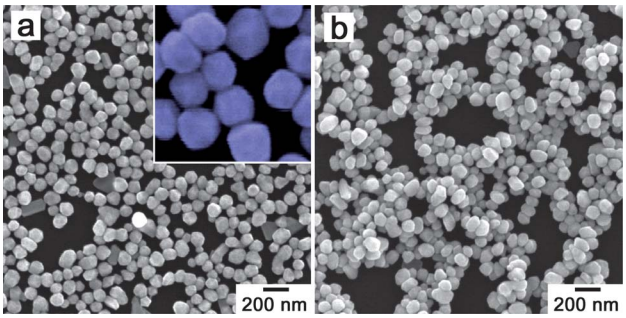

Fig. 6 SEM images of gold mesoparticles synthesized with lower AA concentration (20 mM) after adding different CTAB concentrations: (a) 20 mM, and (b) 40 mM. The gold precursor concentrations are 20 mM.

attach to each other to form short chains (Fig. 6 and S7†). As suggested by Yang *et al.*, this phenomenon can be attributed to a 'glue' function of CTAB molecules, which could serve as the 'glue' that can link the facets of Au NPs into short chains or aggregates.[54,55]

When the AA concentration was increased to 100 mM (the same as in Fig. 2), the presence of CTAB in the pentanol phase (20 mM) would lead to a size decrease of polyhedral nanoparticles to about 70 nm, on the other hand CTAB obviously spurred the aggregation of Au NPs to form chain-like structures (Fig. S8a, b†). When the amount of CTAB was doubled, the particle aggregates overgrew into flower-like structures (Fig. S8b, c†).

When the AA concentration was further increased to 1 M, while the concentration of CTAB remained at 40 mM, flower-like mesoparticles with average size about 400 nm were obtained (Fig. 7a and S9†). The highly textured flower-like Au mesoparticles appear to comprise up to ~100 disc-like tips having lengths of 50–100 nm and base thicknesses of ~15 nm. This dendritic growth can be improved by further increasing the CTAB concentration, while keeping the AA concentration at 1 M. As shown in Fig. 7b–d, the petals of the Au flowers grow from 50–100 nm to more than 1 μm in length by increasing the CTAB concentration from 40 to 160 mM. It is notable that all of the different products described above demonstrate relatively narrow size distributions and uniform morphology (Fig. 7 and S10–S12†).

3.3 Mechanism discussions in morphology evolution

Fig. 8 illustrates the morphology evolution of gold mesoparticles with the change of experimental parameters. When CTAB was absent from the pentanol phase, the increase of AA concentration (conditions of 1–3 in Fig. 8) induced the morphology transformation from star-like to sea urchin-like and even to tiny NPs aggregated in meatball-like shapes. The increase in the concentration of gold ions (conditions of 4, 5 in Fig. 8) would induce the formation of meatball-like mesoparticles with larger sizes. With the presence of CTAB in the pentanol phase, the polyhedral and flower-like mesoparticles were obtained by changing both AA and CTAB concentrations (conditions of 6, 7 in Fig. 8).

In the current oil/water interface synthesis, the gold precursor and reducing agent are separated in the upper and lower solution layers respectively. Only when the gold precursor diffuses into the vicinity of the interface, does it have the chance to be reduced. Thus in this situation, the gold precursors are gradually reduced through gold ions diffusing to the interface gently. Similar to Xie's report,[37] four steps are involved in this growth process, which can be described by a Lamer curve as shown in Fig. S13a.†[10,56] At the first step, the Au ions are reduced into atoms (Fig. 1b), thus the atom concentration at the oil/water interface increases accordingly. At the second step, when the concentration of Au atoms exceeds the supersaturation point, the atoms begin to nucleate *via* the mechanism of self-(or homogeneous) nucleation.[10] The third step involves the nuclei growing into primary NPs, and at the same time, the primary NPs aggregate into mesoparticles with an OA mechanism. The mesoparticles formed with particle-mediated growth show rough surfaces. The NP-built tips on the rough surface prefer to further overgrow into spike-coated structures owing to the protuberant tips being more easily able to capture gold ions or atoms for growth.[57]

The reaction mechanism is schematically illustrated in Fig. S13b.† The Au ions diffuse into the vicinity of the oil/water interface and are subsequently reduced and deposited on the protuberant tips on the particle surface. If an Au ion diffuses into the vicinity of the interface and does not meet reducing agent within a certain period of time, it will diffuse off the interface and not be reduced. Hence, the increases of Au ion and AA concentrations both will induce the increase of reaction rate and higher Au atom concentration will be generated at the first step. According to the higher atom concentration leading to a large number of nuclei with smaller critical nucleus size,[10,58] at conditions of 2, 4, 5 in Fig. 8, with Au ion concentration increasing, more nuclei are formed at the first and second steps. Meanwhile, at higher Au ion concentration, the growth of nuclei is also increased. Thus under the conditions of 4 and 5 in Fig. 8, a higher number of larger NPs aggregate to form larger mesoparticles, while at a lower concentration (condition of 2 in Fig. 8), a lower number of smaller NPs aggregate to form smaller mesoparticles (Fig. 4).

In a colloidal particle-mediated growth system, the formed primary NPs keep moving in the liquid phase due to Brownian motion and they collide at a frequency that can be estimated according to the following equation:[59,60]

$$f = kT\rho^{2/3}/3\pi\eta r \quad (1)$$

where ρ is the density of the NP with a radius of r in a solution with viscosity of η, and T is temperature. At lower AA concentration (condition 1 in Fig. 8), as discussed above, only a small number of NPs can be produced at the initial time. Moreover, according to the above equation, they need more time to aggregate. During this process, the NPs will grow with larger sizes. In the third and fourth steps, the larger NPs will aggregate and build as thick tips on the surfaces of star-like mesoparticles. On the other hand, at higher AA concentration (condition 3 in Fig. 8), a large number of smaller NPs will be produced to form small NP-aggregated mesoparticles. At the same time, the Au ions are reduced more quickly at a higher AA concentration, thus fewer Au ions remain after NP aggregation. Therefore, with the increase of AA concentration, smaller spikes are overgrown on the tips of mesoparticle surfaces and the morphology transforms

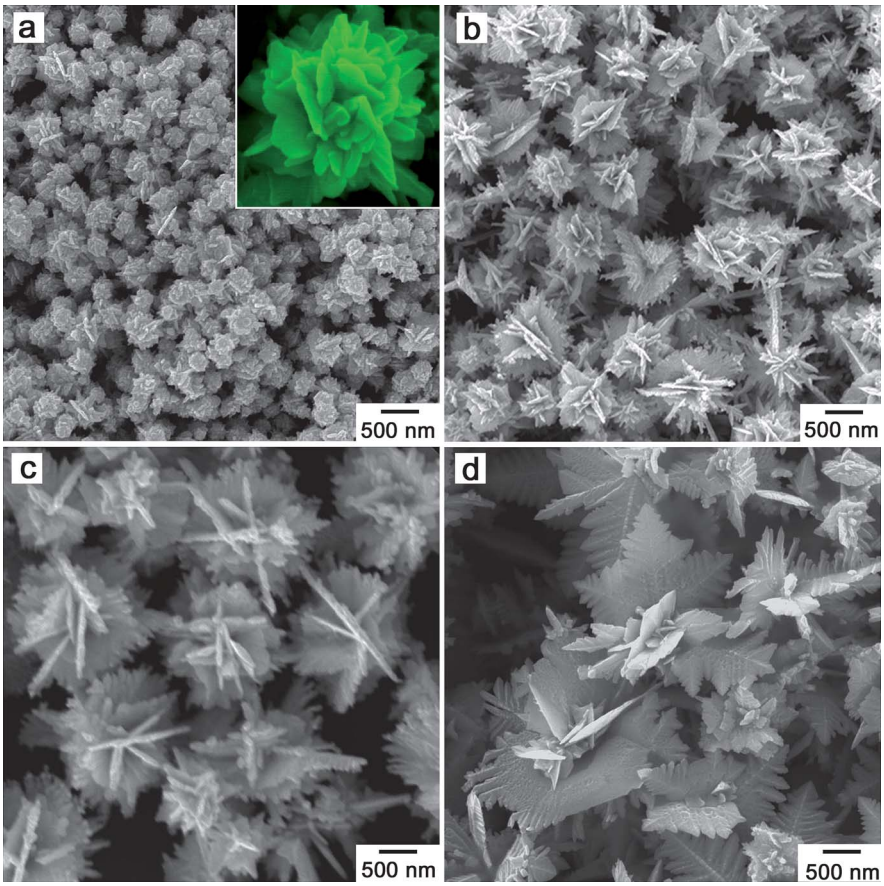

Fig. 7 SEM images of gold mesoparticles synthesized with higher AA concentration (1 M) and different CTAB concentrations: (a) 40 mM, (b) 80 mM, (c) 120 mM, and (d) 160 mM. The gold precursor concentrations are 20 mM.

from star-like to sea-urchin like and even to small-particle-aggregated meatball-like mesoparticles, as shown for conditions 1 to 3 in Fig. 8.

The effect of CTAB molecules on morphology evolution of gold mesoparticles is suggested to follow three roles. First, owing to the formation of Au(III)-CTAB complex, the reducing rate of the gold precursor is retarded and the diffusion of Au ions is also limited.[61,62] Second, the addition of CTAB can prompt the aggregation of primary NPs.[54,55] Third, CTAB can direct Au ions to be preferentially absorbed on the tips, leading to a protuberant growth on the gold mesoparticle surface with higher curvature.[62] At a low AA concentration, the reaction rate is further reduced by addition of CTAB, thus even a small number of larger nuclei are produced in the second step (condition 6 in Fig. 8). According to eqn (1), a small number of NPs are not easy to aggregate and they have enough time to grow. At higher AA concentration (condition 7 in Fig. 8), a larger number of NPs are produced. These NPs are prompted to aggregate by addition of CTAB. At the same time, both the increase of solution viscosity[63] (Fig. S14†) and the formation of an Au(III)-CTAB complex induces the decrease in the diffusing speed of Au ions after CTAB addition, thus more Au ions remain before NP aggregation. At the last step, the remaining Au ions are preferentially captured and overgrown on the tips of mesoparticles to form petals of flower-like mesoparticles, under the directing function of CTAB molecules. With the increase of the CTAB concentrations, more Au ions remain before NP aggregation, subsequently they are induced by CTAB molecules to grow on tips to form larger petals of flower-like mesoparticles or even dendritic mesoparticles.

3.4 Optical and SERS properties of gold mesoparticles

The optical properties of gold mesoparticles with different morphologies are investigated by UV-vis-NIR extinction spectroscopy. Fig. 9a shows the experimentally measured optical extinction spectra of sea urchin-like, flower-like, meatball-like and polyhedral mesoparticles. The monodispersity of the mesoparticles allows the experimental observation of well-defined higher-order multipole plasmon modes in addition to the dipole resonance. For the polyhedral mesoparticles, only one peak corresponding to higher-order multipole resonance (quadrupole located at ~665 nm) is observed, while the dipole peak is located at ~797 nm. For the sea urchin-like, flower-like and meatball-like mesoparticles, three peaks corresponding to higher-order multipole resonances (hexadecapole, octopole and quadrupole) are clearly observed in the spectrum in addition to the dipole resonance. The sea urchin-like and flower-like mesoparticles show similar plasmon resonance models and their extinction peaks are located at ~562/~596 nm (hexadecapole), ~792/~782 nm (octopole), ~998/~983 nm (quadrupole) and ~1196/~1216 nm (dipole) respectively. Our previous report shows that the higher-order multipole extinction peaks of Au

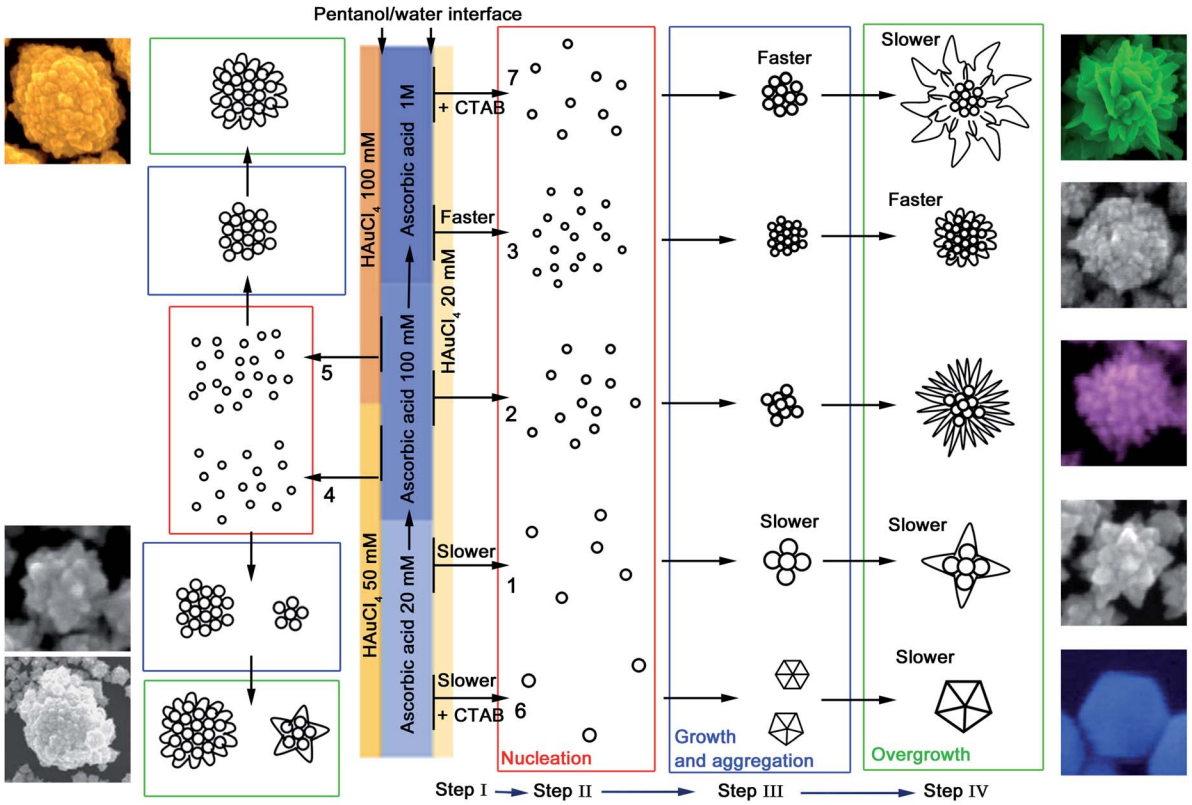

Fig. 8 Schematic illustration of the morphological evolution of gold mesoparticles under different synthesis conditions.

sea urchin-like mesoparticles are located at ~580 nm, ~790 nm and ~980 nm,[23] which matched well with the current result. For the meatball-like mesoparticles, the extinction peaks are located at ~546 nm, ~772 nm, ~889 nm, and ~1460 nm. Compared with sea urchin-like and flower-like mesoparticles, the hexadecapole and qaudrupole extinction peaks shift toward the left and the dipole shifts toward the right. The result also matches well with reported experiment and theory results (their extinction peaks are located at ~520 nm, ~756 nm, ~925 nm and ~1500 nm).[26]

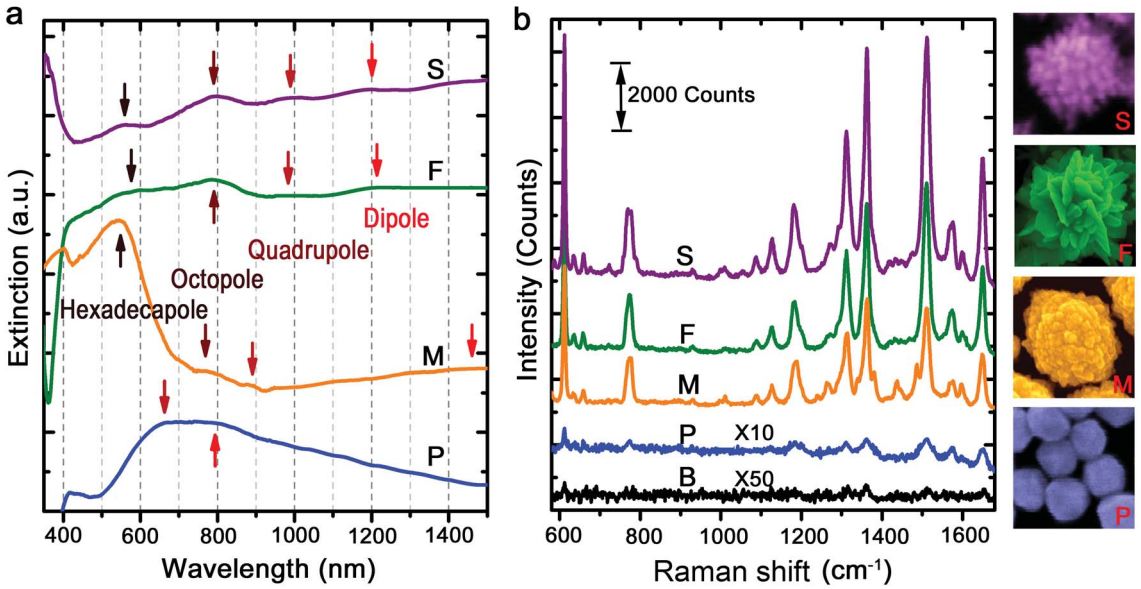

Fig. 9 Optical and SERS properties of gold mesoparticles with different morphologies. (a) UV-vis-NIR spectra. (b) SERS spectrum of R-6G adsorbed on the surface of the substrates contributed by different gold mesoparticle films: S: sea urchin-like, F: flower-like, M: meatball-like, and P: polyhedral. B indicates 'background'.

The SERS performance of the different morphology mesoparticles were evaluated using rhodamine 6G (R6G) molecules as the adsorbate. Fig. 9b shows the SERS signal intensities using a He–Ne laser ($\lambda = 633$ nm) as the excitation source. The intense Raman signals at about 1647, 1506 and 1357 cm^{-1} arise from the totally symmetric modes of in-plane C–C stretching vibrations, which are in agreement with previous reports in both experimental and theoretical investigations.[64,65] Using the reported methods,[23] the SERS enhancement factors of the four kinds of mesostructural substrates are estimated. The sea urchin-like mesostructures show the highest enhancement on the order of $\sim10^7$–10^8. The flower-like and meatball-like mesocrystals show a relatively lower enhancement on the order of $\sim10^6$–10^7. These results are consistent with our previous work and Wang's reports,[23,26] in which the SERS enhancements of individual sea urchin-like mesoparticles and meatball-like mesoparticles are on the order of $\sim10^7$ and 10^6–10^7, while for well arrayed substrates their enhancements are on the order of $\sim10^8$–10^9 and 10^7–10^8, respectively. Maybe since the mesoparticles are not arrayed very well, the enhancements in the current work are higher than those reported for individual mesoparticles but lower than for well arrayed substrates. Based on the discrete dipole approximation (DDA) calculation of the local eclectic field intensity around the modeled sea urchin-like gold mesoparticles in our previous work, the most localized and enhanced electric field areas are found in the vicinity of spikes and longer spikes induce stronger electric field enhancement.[23] In the current case, the sea urchin-like mesoparticles exhibit the highest electric field enhancement which should be due to the density of spikes (number of spikes per area) on sea urchin-like mesoparticles being much higher than that of flower-like mesoparticles, and their surface roughness is higher than that of meatball-like mesoparticles. Thus the sea urchin-like structure is clearly favored as the one potentially demonstrating the largest SERS enhancement. For the polyhedral mesoparticles, their smooth surface theoretically leads to a low electric field enhancement, thus they show a weak SERS enhancement on the order of $\sim10^5$, which is mainly contributed by the aggregation of particles.[53]

4. Conclusions

An oil/water interface synthesis method is developed to prepare gold mesoparticles with various morphologies including sea urchin-like, flower-like, meatball like, star-like, dendritic and polyhedral mesoparticles. Four steps are suggested to explain the growth process of various mesoparticles: atom generation, nucleation, aggregation with an oriented attachment mechanism, and rough surface mediated overgrowth. The concentrations of reducing agent, gold precursor and CTAB show important influences on the morphologies of mesocrystals. The concentrations of reducing agent and gold precursor mainly change the reaction rates and thus induce the morphology transformation. The addition of CTAB has three effects on morphology evolution: promoting NPsaggregation, retaining part of the Au ions unreduced before NP aggregation, and directing Au ions to overgrow on tips of mesoparticles. The highly textured morphologies of the sea urchin-like, flower-like and meatball-like mesoparticles induce more higher-order multipole plasmon modes than polyhedral mesoparticles. The densely packed spike-covered sea urchin-like mesoparticles exhibit the highest SERS sensitivity, and they appear to be very promising as high-performance SERS substrates. Our studies are expected to help people deeply understand not only the particle-mediated growth process for the formation of various types of mesostructures but also the interaction between light and plasmons in these structures at the nanoscale.

Acknowledgements

This work was supported by National Natural Science Foundation of China (Nos. 51071116, 50901056 and 51171139), Doctoral Fund for New Teachers (No. 20090201120053) and the Fundamental Research Funds for the Central Universities. J.X.F. is supported by Tengfei Talent Project of Xi'an Jiaotong University, the New Century Excellent Talents in University (NCET), the Fundamental Research Funds for the Central University (No. 08142008).

Notes and references

1 J. F. Li, Y. F. Huang, Y. Ding, Z. L. Yang, S. B. Li, X. S. Zhou, F. R. Fan, W. Zhang, Z. Y. Zhou, D. Y. Wu, B. Ren, Z. L. Wang and Z. Q. Tian, *Nature*, 2010, **464**, 392.
2 S. M. Nie and S. R. Emery, *Science*, 1997, **275**, 1102.
3 Y. W. C. Cao, R. C. Jin and C. A. Mirkin, *Science*, 2002, **297**, 1536.
4 J. N. Anker, W. P. Hall, O. Lyandres, N. C. Shah, J. Zhao and R. P. Van Duyne, *Nat. Mater.*, 2008, **7**, 442.
5 X. M. Qian, X. H. Peng, D. O. Ansari, Q. Yin-Goen, G. Z. Chen, D. M. Shin, L. Yang, A. N. Young, M. D. Wang and S. M. Nie, *Nat. Biotechnol.*, 2008, **26**, 83.
6 D. Graham, D. G. Thompson, W. E. Smith and K. Faulds, *Nat. Nanotechnol.*, 2008, **3**, 548.
7 Z. Chen, S. M. Tabakman, A. P. Goodwin, M. G. Kattah, D. Daranciang, X. R. Wang, G. Y. Zhang, X. L. Li, Z. Liu, P. J. Utz, K. L. Jiang, S. S. Fan and H. J. Dai, *Nat. Biotechnol.*, 2008, **26**, 1285.
8 M. T. Sun, B. S. Wan, Y. J. Liu, Y. Jia and H. X. Xu, *J. Raman Spectrosc.*, 2008, **39**, 402.
9 M. T. Sun, S. S. Liu, M. D. Chen and H. X. Xu, *J. Raman Spectrosc.*, 2009, **40**, 137.
10 Y. N. Xia, Y. J. Xiong, B. Lim and S. E. Skrabalak, *Angew. Chem., Int. Ed.*, 2009, **48**, 60.
11 Z. Q. Tian, B. Ren and D. Y. Wu, *J. Phys. Chem. B*, 2002, **106**, 9463.
12 H. X. Xu, J. Aizpurua, M. Kall and P. Apell, *Phys. Rev. E: Stat. Phys., Plasmas, Fluids, Relat. Interdiscip. Top.*, 2000, **62**, 4318.
13 Z.-Y. Li and Y. N. Xia, *Nano Lett.*, 2010, **10**, 243.
14 S. E. J. Bell and N. M. S. Sirimuthu, *Chem. Soc. Rev.*, 2008, **37**, 1012.
15 H. X. Xu, E. J. Bjerneld, M. Kall and L. Borjesson, *Phys. Rev. Lett.*, 1999, **83**, 4357.
16 A. M. Michaels, J. Jiang and L. Brus, *J. Phys. Chem. B*, 2000, **104**, 11965.
17 M. J. Mulvihill, X. Y. Ling, J. Henzie and P. D. Yang, *J. Am. Chem. Soc.*, 2010, **132**, 268.
18 W. H. Zhang, X. D. Cui, B. S. Yeo, T. Schmid, C. Hafner and R. Zenobi, *Nano Lett.*, 2007, **7**, 1401.
19 M. Rycenga, X. H. Xia, C. H. Moran, F. Zhou, D. Qin, Z. Y. Li and Y. N. Xia, *Angew. Chem., Int. Ed.*, 2011, **50**, 5473.
20 Y. Fang, N. H. Seong and D. D. Dlott, *Science*, 2008, **321**, 388.
21 M. F. Mrozek, D. Zhang and D. Ben-Amotz, *Carbohydr. Res.*, 2004, **339**, 141.
22 C. L. Haynes, A. D. McFarland and R. P. Van Duyne, *Anal. Chem.*, 2005, **77**, 338a.
23 J. X. Fang, S. Y. Du, S. Lebedkin, Z. Y. Li, R. Kruk, M. Kappes and H. Hahn, *Nano Lett.*, 2010, **10**, 5006.
24 D. K. Lim, K. S. Jeon, J. H. Hwang, H. Kim, S. Kwon, Y. D. Suh and J. M. Nam, *Nat. Nanotechnol.*, 2011, **6**, 452.
25 H. Y. Liang, Z. P. Li, W. Z. Wang, Y. S. Wu and H. X. Xu, *Adv. Mater.*, 2009, **21**, 4614.
26 H. Wang and N. J. Halas, *Adv. Mater.*, 2008, **20**, 820.

27 S. Maksimuk, X. Teng and H. Yang, *J. Phys. Chem. C*, 2007, **111**, 14312.
28 B. Lim, J. G. Wang, P. H. C. Camargo, C. M. Cobley, M. J. Kim and Y. N. Xia, *Angew. Chem., Int. Ed.*, 2009, **48**, 6304.
29 Z. D. Wang, J. Q. Zhang, J. M. Ekman, P. J. A. Kenis and Y. Lu, *Nano Lett.*, 2010, **10**, 1886.
30 Y. J. Li and Y. Huang, *Adv. Mater.*, 2010, **22**, 1921.
31 J. P. Xie, J. Y. Lee and D. I. C. Wang, *Chem. Mater.*, 2007, **19**, 2823.
32 H. J. You, J. X. Fang, F. Chen, M. Shi, X. P. Song and B. J. Ding, *J. Phys. Chem. C*, 2008, **112**, 16301.
33 J. X. Fang, H. J. You, C. Zhu, P. Kong, M. Shi, X. P. Song and B. J. Ding, *Chem. Phys. Lett.*, 2007, **439**, 204.
34 S. Cheong, J. Watt, B. Ingham, M. F. Toney and R. D. Tilley, *J. Am. Chem. Soc.*, 2009, **131**, 14590.
35 S. D. Sun, H. J. You, C. C. Kong, X. P. Song, B. J. Ding and Z. M. Yang, *CrystEngComm*, 2011, **13**, 2837.
36 X. W. Teng, S. Maksimuk, S. Frommer and H. Yang, *Chem. Mater.*, 2007, **19**, 36.
37 J. P. Xie, Q. B. Zhang, J. Y. Lee and D. I. C. Wang, *ACS Nano*, 2008, **2**, 2473.
38 H. M. Zheng, R. K. Smith, Y. W. Jun, C. Kisielowski, U. Dahmen and A. P. Alivisatos, *Science*, 2009, **324**, 1309.
39 T. X. Wang, H. Colfen and M. Antonietti, *J. Am. Chem. Soc.*, 2005, **127**, 3246.
40 J. X. Fang, B. J. Ding and H. Gleiter, *Chem. Soc. Rev.*, 2011, **40**, 5347.
41 R. L. Penn and J. F. Banfield, *Science*, 1998, **281**, 969.
42 H. Colfen and M. Antonietti, *Angew. Chem., Int. Ed.*, 2005, **44**, 5576.
43 A. W. Xu, M. Antonietti, H. Colfen and Y. P. Fang, *Adv. Funct. Mater.*, 2006, **16**, 903.
44 B. W. Lim, X. M. Lu, M. J. Jiang, P. H. C. Camargo, E. C. Cho, E. P. Lee and Y. N. Xia, *Nano Lett.*, 2008, **8**, 4043.
45 M. Nogami, R. Koike, R. Jalem, G. Kawamura, Y. Yang and Y. Sasaki, *J. Phys. Chem. Lett.*, 2010, **1**, 568.
46 J. X. Fang, H. J. You, P. Kong, Y. Yi, X. P. Song and B. J. Ding, *Cryst. Growth Des.*, 2007, **7**, 864.
47 J. P. Xiao, Y. Xie, R. Tang, M. Chen and X. B. Tian, *Adv. Mater.*, 2001, **13**, 1887.
48 B. Lim, M. J. Jiang, P. H. C. Camargo, E. C. Cho, J. Tao, X. M. Lu, Y. M. Zhu and Y. A. Xia, *Science*, 2009, **324**, 1302.
49 S. J. Guo, S. J. Dong and E. W. Wang, *ACS Nano*, 2010, **4**, 547.
50 W. R. Zhu, X. P. Zhao and J. Q. Guo, *Appl. Phys. Lett.*, 2008, **92**, 241116.
51 H. B. Xia and D. Y. Wang, *Adv. Mater.*, 2008, **20**, 4253.
52 X. J. Yu, L. N. Zhuan, S. C. Yang, Z. M. Yang, X. P. Song and B. J. Ding, *Colloids Surf., A*, 2010, **372**, 22.
53 S. C. Yang, X. W. Wan, Y. T. Ji, L. Q. Wang, X. P. Song, B. J. Ding and Z. M. Yang, *CrystEngComm*, 2010, **12**, 3291.
54 Y. Yang, S. Matsubara, M. Nogami, J. L. Shi and W. M. Huang, *Nanotechnology*, 2006, **17**, 2821.
55 Y. Yang, J. L. Shi, T. Tanaka and M. Nogami, *Langmuir*, 2007, **23**, 12042.
56 V. K. Lamer and R. H. Dinegar, *J. Am. Chem. Soc.*, 1950, **72**, 4847.
57 H. J. You, C. H. Ding, X. P. Song, B. J. Ding and J. X. Fang, *CrystEngComm*, 2011, **13**, 4491.
58 Z. M. Peng and H. Yang, *Nano Today*, 2009, **4**, 143.
59 A. Halder and N. Ravishankar, *Adv. Mater.*, 2007, **19**, 1854.
60 Z. M. Peng, H. J. You and H. Yang, *ACS Nano*, 2010, **4**, 1501.
61 K. Torigoe and K. Esumi, *Langmuir*, 1992, **8**, 59.
62 J. Perez-Juste, L. M. Liz-Marzan, S. Carnie, D. Y. C. Chan and P. Mulvaney, *Adv. Funct. Mater.*, 2004, **14**, 571.
63 S. Shim, C. M. Stuart and R. A. Mathies, *ChemPhysChem*, 2008, **9**, 697.
64 H. J. You, J. X. Fang, F. Chen, C. Zhu, X. P. Song and B. J. Ding, *Chem. Phys. Lett.*, 2008, **465**, 131.
65 J. A. Dieringer, K. L. Wustholz, D. J. Masiello, J. P. Camden, S. L. Kleinman, G. C. Schatz and R. P. Van Duyne, *J. Am. Chem. Soc.*, 2009, **131**, 849.

